

# Experimental and theoretical investigation of the fluid behavior during polymeric fiber formation with and without pressure

Cite as: Appl. Phys. Rev. **6**, 041401 (2019); <https://doi.org/10.1063/1.5110965>

Submitted: 22 May 2019 . Accepted: 09 September 2019 . Published Online: 15 October 2019

Hussain Alenezi , Muhammet Emin Cam , and Mohan Edirisinghe 

## COLLECTIONS

 This paper was selected as Featured



View Online



Export Citation



CrossMark

## ARTICLES YOU MAY BE INTERESTED IN

[The rationale and emergence of electroconductive biomaterial scaffolds in cardiac tissue engineering](#)

APL Bioengineering **3**, 041501 (2019); <https://doi.org/10.1063/1.5116579>

[Recent progress in ultrafast lasers based on 2D materials as a saturable absorber](#)

Applied Physics Reviews **6**, 041304 (2019); <https://doi.org/10.1063/1.5099188>

[Distributed optical fiber sensing: Review and perspective](#)

Applied Physics Reviews **6**, 041302 (2019); <https://doi.org/10.1063/1.5113955>



## Applied Physics Reviews

First Original Research Articles  
NOW ONLINE!

READ  
NOW!

# Experimental and theoretical investigation of the fluid behavior during polymeric fiber formation with and without pressure

Cite as: Appl. Phys. Rev. 6, 041401 (2019); doi: 10.1063/1.5110965

Submitted: 22 May 2019 · Accepted: 9 September 2019 ·

Published Online: 15 October 2019



View Online



Export Citation



CrossMark

Hussain Alenezi,<sup>1,2</sup>  Muhammet Emin Cam,<sup>1,3,4</sup>  and Mohan Edirisinghe<sup>1,a)</sup> 

## AFFILIATIONS

<sup>1</sup>Department of Mechanical Engineering, University College London, Torrington Place, London WC1E 7JE, United Kingdom

<sup>2</sup>Department of Manufacturing Engineering, College of Technological Studies, PAAET, 13092 Kuwait City, Kuwait

<sup>3</sup>Center for Nanotechnology and Biomaterials Research, Marmara University, Istanbul 34722, Turkey

<sup>4</sup>Department of Pharmacology, Faculty of Pharmacy, Marmara University, Istanbul 34668, Turkey

<sup>a)</sup> Author to whom correspondence should be addressed: [m.edirisinghe@ucl.ac.uk](mailto:m.edirisinghe@ucl.ac.uk)

## ABSTRACT

The fabrication of polymeric micro/nanofibers is gaining attention due to their use in an array of applications including tissue engineering scaffolds, nanosensors, and fiber-reinforced composites. Despite their versatile nature, polymeric fibers are widely underutilized due to the lack of reliable, large-scale production techniques. Upon the discovery of centrifugal spinning and, recently, pressurized gyration techniques, new research directions have emerged. Here, we report a comprehensive study detailing the optimal conditions to significantly improve the morphology, homogeneity, and yield of fibers of varying diameters. A series of polymeric fibers was created using a 21 wt. % solution of polyethylene oxide in distilled water and the fluid behavior was monitored inside a transparent reservoir using a high-speed camera. Fabrication of the fibers took less than 1 s. Using centrifugal spinning, we studied the formation of the fibers at three different rotational speeds, and for pressurized gyration, one rotational speed was studied with three different nitrogen gas pressures. Using the pressurized gyration technique at a gas pressure of 0.3 MPa, there was significant improvement in the production yield of the fibers. We found a strong correlation between the variation of pressure and the rate of the solution leaving the reservoir with the improved morphology of the fibers. The use of reduced power techniques, like centrifugal spinning and pressured gyration, to yield high-quality nonwoven nanofibers and microfibers in large quantities is important due to their use in rapidly expanding markets.

© 2019 Author(s). All article content, except where otherwise noted, is licensed under a Creative Commons Attribution (CC BY) license (<http://creativecommons.org/licenses/by/4.0/>). <https://doi.org/10.1063/1.5110965>

## I. INTRODUCTION

In recent years, naturally based and synthetic polymeric nanofibers have become widely used in both research and manufacturing applications.<sup>1</sup> Their high porosity and superlative mechanical properties, as well as their substantial ratio of volume to the surface area, make polymeric nanofibers attractive for potential applications such as catalyst supports, composite reinforcements, protective clothing, tissue-engineered scaffolds, and nanosensors. One example of a potential application is the differentiation between peripheral nerves and tendon cells.<sup>2</sup> Although nanofibers are versatile, their utilization remains limited by the insufficient reliable quantity-production techniques.<sup>3</sup>

Several manufacturers have been extensively involved in the global marketplace of the fiber industry.<sup>4</sup> Nonwoven filter media are a subcategory of this industry that has contributed to market growth.

According to a global market report by BCC Research, this growth is forecast to progress from almost \$5.1B in 2018 to \$6.5B by 2023, which indicates a compound annual growth rate (CAGR) of 5% between 2018 and 2023.<sup>5</sup> In global markets, nanofiber products were predicted to grow from \$92M in 2018 to \$4.3B by 2023 at a CAGR of 36.2% between 2018 and 2023.<sup>6</sup> These statistics are inclusive of every manufacturing technique associated with nanofiber and microfiber nonwoven filter media. It is difficult to obtain authentic data exclusively to nanofiber markets; however, with the development of future applications in the market place, we could observe a connection with the expanding microfiber industry.

At present, it is possible to apply many techniques to produce both nanoscale and microscale fibers.<sup>7</sup> These techniques include melt blowing,<sup>8</sup> phase separation,<sup>9</sup> electrospinning,<sup>10</sup> drawing,<sup>11</sup> template

synthesis,<sup>12</sup> and island-in-the-sea spinning.<sup>13</sup> Several of these techniques have disadvantages, such as the use of large amounts of energy to produce fiber or a low rate of production.<sup>14</sup> We require a more effective system to generate submicron fibers and nanofibers, leading to reduced power consumption and greater production rates. Such requirements could be satisfied by applying centrifugal spinning (CS) and pressurized gyration (PG) techniques.

CS, which is sometimes referred to as rotary jet spinning (RJS) or force spinning,<sup>15</sup> is comprised of a reservoir that contains polymer solutions attached to a motor. The rate at which the reservoir is spun about its symmetrical axis is established by the balance between centrifugal and capillary forces; where this rate is more significant than this threshold, one or many of the small openings attached to the reservoir wall eject a viscous jet of solvent.<sup>16</sup> As the solvent evaporates, this jet is projected outwards in a spiral trajectory due to the comparatively high surface area. During this process, centrifugal forces extend the reach of this jet. The rate of evaporation of the solvent depends upon its diffusion coefficient through the polymer, with the jet traveling until it arrives at the stationary collector's walls. From there, the remaining solvent evaporates, and the fibers solidify, enabling them to be gathered. It is essential to satisfy a crucial minimum rotational speed for fiber formation, below which no polymer jet exists, and it is impossible for the centrifugal force to overcome the surface tension.<sup>17,18</sup> If rotational speeds are low while the vessel accelerates, the low surface tension of the solvent may cause it to separate from the polymer. In this situation, it is not usual for a polymer jet to form; consequently, the surrounding collection walls lose the solvent. Therefore, the appropriate rotation speed is necessary to produce a polymer jet and the subsequent fiber formation, thereby affecting the morphology of such fibers.<sup>7,19,20</sup>

PG, which was invented in 2013, functions by manipulating a selected polymer solution's Rayleigh–Taylor instability.<sup>17</sup> The rotational speed increases rapidly as the motor starts, which causes the centrifugal force to increase; in turn, this increased force leads to the displacement of the polymer solution. A pressure differential is created in the vessel because of the applied gas pressure acting against the liquid, thereby forcing the solution out. The principal driver behind the liquid extrusion through the vessel openings is the centrifugal force, which is generated due to the surface tension gradient on the liquid-air interface. Furthermore, this gradient prompts Marangoni stress tangential to the liquid-gas interface, thus initiating flow at the tip of the polymer droplet.<sup>20,21</sup> Fibers are generated by centrifugal force, which continuously stretches the polymer jet as it leaves the perforations; additionally, the gas inlet at the openings generates the pressure differential. Slowly, evaporation causes loss of solvent, and the source of the fiber strand is the extruded polymer that remains in the jet. Ultimately, the dried fiber is deposited on the adjacent collection walls, and a bundle of fibers is formed by the rapid repetition of this procedure.<sup>17</sup>

Various polymers have been using various techniques; this includes natural polymers, such as alginate, chitosan collagen, gelatin, and starch, and synthetic polymers, such as poly(glycolic acid) (PGA), poly( $\epsilon$ -caprolactone) (PCL), poly(lactic-co-glycolic acid) (PLGA), poly(lactic acid) (PLA), and fabricated scaffolds with desired properties.<sup>22</sup> During this experiment, we utilized polyethylene oxide (PEO) because it is among the most extensively examined water-soluble synthetic polymer, both from the fundamental viewpoint of understanding how polymer solutions behave and from the broad scope of its applications.<sup>23</sup>

Several researchers worldwide have recently studied the control of the operational conditions of PG and CS to manufacture nanoscale fibers.<sup>24</sup> We studied fiber diameter control with every available processing method. Modeling, which has many advantages in refining and enhancing the procedure, provides useful knowledge for comprehending this procedure in greater detail. However, this technique is not always possible due to the unique application of experimental methods. The following fundamental parameters are utilized in modeling PG and CS procedures: air drag, centrifugal force, Coriolis force, spinning speed, polymer viscosity, evaporation time of the solvent in the collector during the spinning process, and the pressure applied on the fiber.<sup>25</sup> The complicated nature of the RJS procedure is clearly outlined in the many publications that examine the forming techniques and viscoelastic properties of RJS, and also supply helpful instructions for future RJS paradigms.

The behavior of polymer solutions within a reservoir using the PG and CS techniques, as well as other similar techniques, is not analyzed in the literature. This study investigates the behavior of a viscous polymer solution within a transparent reservoir, which has multiple narrow (0.5 mm) perforations at a central position in the reservoir, allowing an observer to visualize the behavior of the solution inside the vessel at millisecond intervals in the course of CS and PG. We investigated the impact of rotation speed at 7000, 8500, and 10 000 rpm on the solution ejected from the openings during CS; the impact of the pressure,  $P$ , at various spinning speeds,  $\omega$ , in the PG technique; and the effect of pressurized gas in controlling the behavior of the fluid within the vessel in decreasing the production time. For comparative study, we used computational fluid dynamics (CFD) for numerical analysis of the fluid flow within the vessel, and we used still shots captured by a high-speed camera to record both experimental processes.

## II. MATERIALS AND METHODS

### A. Materials

In this investigation, PEO,  $\overline{M}_w 2 \times 10^5 \text{ g mol}^{-1}$ , which was used as the polymer, was purchased from Sigma Aldrich (Poole, UK). Distilled water was used as a solvent.

### B. Preparation and characterization of solutions

PEO was completely dissolved at concentration 21 wt.% in distilled water. This concentration was selected based on our previous work.<sup>17</sup> The polymer solution was magnetically stirred for 24 h and kept at ambient temperature ( $\approx 25^\circ\text{C}$ ). Physical parameters, such as the viscosity and surface tension of the solutions, were measured by a viscometer (Brookfield DV-111, Harlow, UK) and a force Tensiometer (KRÜSS K9, Hamburg, Germany), respectively. The measurements were repeated three times at ambient temperature ( $25^\circ\text{C}$ ), and the equipment was calibrated before the measurements.

### C. Transparent vessel specifications

The experimental setup consisted of a transparent reservoir, herein referred to as Mark I; the Mark I cylinder had a 60-mm outer diameter and a 58-mm inner diameter, with perforations of 0.5 mm diameter positioned along the circumference halfway up the cylinder. The top of the cylinder was attached to a transparent lid with a hole in the center for the inlet gas (nitrogen).

## D. High-speed camera

The fluid behavior within the reservoir was observed using still shots from a high-speed camera (Photron, FASTCAM SA1.1, Tokyo, Japan), which captured 5400 frames per second.

## E. Fiber forming and characterization

The changes in the fiber size, morphology and production yield of PEO fibers using CS at three different speeds (7000, 8500, and 10 000 rpm) and using PG at three different gas pressures (0.1, 0.2, and 0.3 MPa, speed kept constant at 10 000 rpm) were investigated using scanning electron microscopy (Hitachi VP-SEM S-3400N). The accelerating voltage used for the SEM was 5 kV. The temperature and relative humidity for all spinning experiments were 25 °C and 48%, respectively. The surface of the samples was coated with gold for 60 s. The average fiber diameter and their size distribution were determined by measuring 100 fibers in randomly recorded SEM micrographs using image software ImageJ (Brocken Symmetry Software). The yield was measured by measuring the mass of fibers spun using 1 ml of the polymer solution.

## F. Design of experiments

In this investigation, the reservoir was filled with a PEO solution to a height of 5 mm to obtain a more systematic understanding of the forming conditions. Another aim was to establish a qualitative basis for the analysis of relationships between the high-speed spinning in CS and the effects of pressure gas flow inside the reservoir in PG.

## G. Micropolar fluid theory

In cylindrical coordinates ( $r$ ;  $\theta$ ;  $z$ ) for rotating flow in a cylinder, a function is utilized to describe the motion of the fluid,

$$p - p_0 = -\rho g(z - z_0) + \frac{1}{2}\rho\omega^2 r^2. \quad (1)$$

In the case where there is no change in pressure at the free surface of the rotating fluid at any point,

$$z = z_0 + \left(\frac{\omega^2}{2g}\right)r^2, \quad (2)$$

which is defined as a quadratic function of the free surface; therefore, we expect the free surface of the fluid to assume a parabolic shape when rotated.

The gyration vector is a good parameter for determining the physics at the microscale when adopting the continuum assumption. The balance laws of the micropolar continuum can be expressed as follows.

- Conservation of mass,

$$\rho + \rho v_{l,l} = 0. \quad (3)$$

- Balance of momentum,

$$-\nabla p + (\lambda + \mu)\nabla\nabla v + (\mu + \kappa)\nabla^2 v + \kappa\nabla \times \omega + \rho f = \rho v. \quad (4)$$

- Balance of angular momentum,

$$(\alpha + \beta)\nabla\nabla\omega + \gamma\nabla^2\omega + \kappa(\nabla \times v - 2\omega) + \rho l = \rho l\omega. \quad (5)$$

If the micromotion equals the macromotion, that is, if  $x_l K = x_l K$ , this leads to

$$\omega_m = \frac{1}{2}\varepsilon_{lkm}v_{k,l}, \quad (6)$$

$$-\nabla p + (\lambda + \mu^*)\nabla\nabla v + (\mu^*)\nabla^2 v + \rho f = \rho v \quad \text{and} \quad \mu^* = \mu + \frac{1}{2\kappa}. \quad (7)$$

Compared to the Navier–Stokes equations in micropolar fluid dynamics (MFD), gyration has a more general MFD formulation because it has a similar concept as a spinning solid globe. In this study, the instability between the PEO and the gas interface could be specified by equating the gravitational force per unit volume, which has a disruptive effect, to the surface tension force per unit volume, which has a stabilizing effect,<sup>17</sup>

$$\rho g \frac{\partial h}{\partial x} = \sigma g \frac{\partial^3 h}{\partial^3 x}, \quad (8)$$

where  $\rho$  is the density of the polymer solution,  $g$  is the gravitational force,  $\sigma$  is the PEO–gas surface tension,  $h$  is the height of the PEO drop suspended below the horizontal surface, and  $x$  is the vertical distance.

## H. Equations for two-phase flow

In this study, a simulation was conducted with the flow of nitrogen and a PEO solution inside a rotating cylinder. From a physical standpoint, both nitrogen and PEO can be regarded as fluids that obey the same laws but have different material properties. Therefore, the flow of generic fluid was studied in two phases, where one was comprised of a PEO solution and the other of introduced nitrogen gas. These phases and the mixture of these substances can be described by a so-called phase field,  $\phi$ , that changes from +1 to −1, where  $\phi = +1$  represents the PEO solution and  $\phi = -1$  represents the nitrogen,

$$\phi \cdot \alpha \cdot \nabla \phi - \Upsilon \Delta \phi = 0, \quad (9)$$

$$\theta = -\Gamma \Delta \phi + \frac{\Gamma \phi (\phi^2 - 1)}{\delta^2} = 0. \quad (10)$$

In the two-phase flow, the density  $\rho$  and the viscosity  $\nu$  vary over the domain. Thus, we must be able to track the interface between the nitrogen and PEO solution to determine these parameters

$$\rho(x) = \frac{1}{2} \{ [1 + \phi(x)]\rho_p + [1 - \phi(x)]\rho_{N_2} \}, \quad (11)$$

$$\nu(x) = \frac{1}{2} \{ [1 + \phi(x)]\nu_p + [1 - \phi(x)]\nu_{N_2} \}, \quad (12)$$

where  $\rho_{N_2}$  and  $\rho_p$  are the nominal densities of nitrogen and the PEO solution, respectively, and  $\nu_{N_2}$  and  $\nu_w$  are the corresponding nominal values of the viscosity of nitrogen and PEO, respectively.

## I. Numerical study

A commercially available CFD code (ANSYS-Fluent 19) was used for the numerical calculations to simulate the flow inside the cylinder and at the outlets of the orifices. This was done to investigate the

influence of the rotational speed and pressure, which was applied at the inlet of the 10-mm diameter hole at the top of the cylinder, on the fluid parameters at the holes. The governing equations were solved for the flow, volume fractions, and pressure values at every cell for both phases. The first step was to create a three-dimensional (3D) geometrical model of the case study with CAD software. The second step was mesh generation. The final step was defining the methods and boundary conditions.

### 1. Rotating cylinder

The geometry was set up for the 5 mm height of PEO in the rotating cylinder, including an instance when nitrogen gas filled the cylinder. The fluid starts at rest at the bottom of the cylinder. The bottom then starts rotating the fluid at a constant speed to make a vortex. The walls and top of the cylinder are under slip conditions ( $\Gamma L$ ). To set the rotation, the bottom of the cylinder is under Dirichlet conditions ( $\Gamma D$ ).

### 2. Governing equations

A realizable  $k$ - $\epsilon$  turbulence model was used to simulate turbulent flow. This model, which is the most recently developed of three  $k$ - $\epsilon$  variations, has two main differences from the standard  $k$ - $\epsilon$  model: it uses a new equation for turbulent viscosity and the transport equation for the dissipation rate is derived from that of the fluctuation in mean square vorticity. The form of the eddy viscosity (turbulent) equations is based on the realizability constraints. These are not satisfied by either the standard or re-normalization group theory (RNG)  $k$ - $\epsilon$  models, which makes the realizable model more precise than these models at predicting complex flows involving rotation, recirculation, secondary flow features, strong streamline curvature, and boundary layers under strong adverse pressure gradients.

In this study, after conducting a comparison, finding another suitable solution method for the transient formulation was the first-order implicit scheme and the simple scheme for pressure-speed coupling with spatial discretization. We utilized the least squares cell-based scheme for the gradient, the presto scheme for the pressure, the geo-reconstruct scheme for volume fractions, and the first-order upwind scheme for turbulent kinetic energy.

### 3. Mesh generation

To ensure the validity and accuracy of the numerical results and the independence of the numerical solutions, the grid was carefully checked. Figure 1 illustrates the grid topology used for the 3D grid system. The size of elements was changed until a size was reached that did not affect the results; also, the number of elements differed from 120 325 to 210 681. No change for a solution was found after 189 250 elements, so this study used standard curvature meshes generated by computational fluid dynamic software (FLUENT).

### 4. Initial conditions

For all simulation tests, the cylinder was filled with liquid PEO to a height of 5 mm from the bottom, and the cylinder was assumed to rotate at a constant speed to reduce the processing

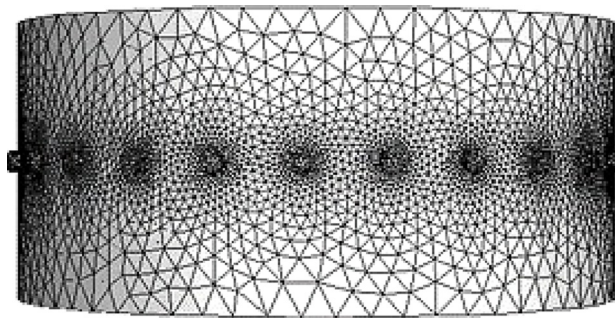


FIG. 1. Grid system for the inner domain of the transparent reservoir.

time. Moreover, to study the effect of nitrogen gas pressure, it was evident that the rotation of the cylinder must remain constant at maximum speed. The surface tension was considered to be  $0.057 \text{ N m}^{-1}$  (see Sec. III A below).

### 5. Boundary conditions

To study the effect of gravity force, the ambient temperature was set at  $25^\circ\text{C}$  and the pressure was set at 0.1 MPa. Different rotation speeds were implemented ( $\omega = 7000, 8500, \text{ and } 10\,000 \text{ rpm}$ ) without the utilization of nitrogen gas; at 10 000 rpm, the nitrogen gas pressure levels applied in the tests were 0.1, 0.2, and 0.3 MPa. The gas inlet at the top of the cylinder was a 10-mm diameter hole.

## III. RESULTS AND DISCUSSION

### A. Physical properties of PEO solution

The viscosity was  $3000 \pm 30 \text{ N m}^{-1}$  and the surface tension was  $57 \pm 5 \text{ mN m}^{-1}$ .

### B. Spinning fibers

#### 1. CS at 7000, 8500, and 10 000 rpm

*a. CS at 7000 rpm.* Figure 2(a) shows the vessel at rest during the process; in this high-speed camera video frame, it can be observed that the PEO solution has started to spin. Due to the manual starting of the experiment, there was a difference between the start time of the camera and the motor; therefore, in the following figures depicting an angular velocity of  $\omega = 0$ , the time registration in the first still video picture will be considered equal to zero. The fluid behavior is shown in Fig. 2(b) at  $t \approx 215 \text{ ms}$  since the motor accelerates to achieve the proposed  $\omega$ . The PEO solution arrived at the orifices, but no solution jetted out of the orifices, and it is clear that the fluid profile was parabola-shaped, which indicates that the fluid on the opposite side has almost the same shape. Figure 2(c) illustrates that no fluid jetted out of the reservoir before the solution reached the top surface in the chamber; at this point, the fluid had almost reached the top of the chamber (in the top left corner) at  $t \approx 434 \text{ ms}$ , and the fluid commenced exiting the pot through the orifices on the same side.

*b. CS at 8500 rpm.* Figure 2(d) illustrates the PEO solution at rest,  $t = 0$ , and after this time, the reservoir started to spin. It is clearly

shown in Fig. 2(e) that the spinning accelerated rapidly to achieve the required speed and the fluid profile of the solution behaved unsymmetrically at  $t = 171$  ms. Therefore, a small part of the solution arrived at the orifice, while the rest of the solution remained at the bottom of the chamber and no fluid was jetted. Figure 2(b) shows that the fluid behavior at 7500 rpm was parabolic-shaped and almost all the solution tried to reach the orifices, whereas in Fig. 2(e), the solution climbed the walls on one side. At  $t = 436$  ms, the shape of the fluid was parabolic [Fig. 2(f)]; and the solution started to jet from the orifices on the left-hand side, as shown in Fig. 2(f). Moreover, the time required to stabilize the fluid at 8500 rpm was greater than it was at 7000 rpm. It was clear that the jetted fluid started before the solution arrived at the top surface in the chamber [Fig. 2(c)].

*c. CS at 10 000 rpm.* Figures 2(g), 2(h), and 2(i) illustrate the changes in fluid profile at various times at  $\omega = 10\,000$  rpm. In Fig. 2(g), the solution profile within the reservoir was determined to be at rest when  $t = 0$  ms, while the PEO solution reached the orifices on the left-hand side of the chamber without any jetted solution coming out of the openings.

Moreover, the fluid profile inside the cylinder was unsymmetrical, as most of the fluid had not arrived at the orifices yet because it had not reached the required rotation speed. In contrast, the fluid shown in Fig. 2(i) behaved in accordance with the asymmetric profile of parabolic shape, and it is clearly shown that the solution started

jetting from one of the orifices on the left-hand side of the chamber although the rest of the orifices had not jetted any solution. Also, the solution jetted before arriving at the top surface of the cylinder, which contrasts with the application of  $\omega = 7000$  and 8500 rpm.

## 2. PG at 10 000 rpm with 0.1, 0.2, and 0.3 MPa inlet gas

*a. PG with 0.1 MPa.* Figures 3(a), 3(b), and 3(c) show the PEO solution profile at 0.1 MPa of inlet pressure at various times (at rest,  $t = 187$  ms, and  $t = 371$  ms) at  $\omega = 10\,000$  rpm. Figure 3(a) shows the solution profile at rest, without applying any inlet pressure or rotation. The PEO solution reached all the orifices at almost the same time and moved up the cylinder walls in a controlled movement. Once the PEO solution arrived at the openings, the solution started jetting from the openings. Figure 3(c) confirms that the fluid profile was controlled and moved upward with the same altitude. Moreover, in this case, all the orifices jetted the solution at the same time, volume, and speed with the incorporation of nitrogen gas, which allowed the fluid to jet at high-speed, as will be discussed in the numerical results (Sec. III C 4). The incorporation of nitrogen gas improved the shape, size, and morphology of polymer fibers jetted out of the cylinder (Sec. III D).

*b. PG with 0.2 MPa.* Figures 3(d), 3(e), and 3(f) illustrate the effects of increasing inlet pressure on the behavior of the PEO solution

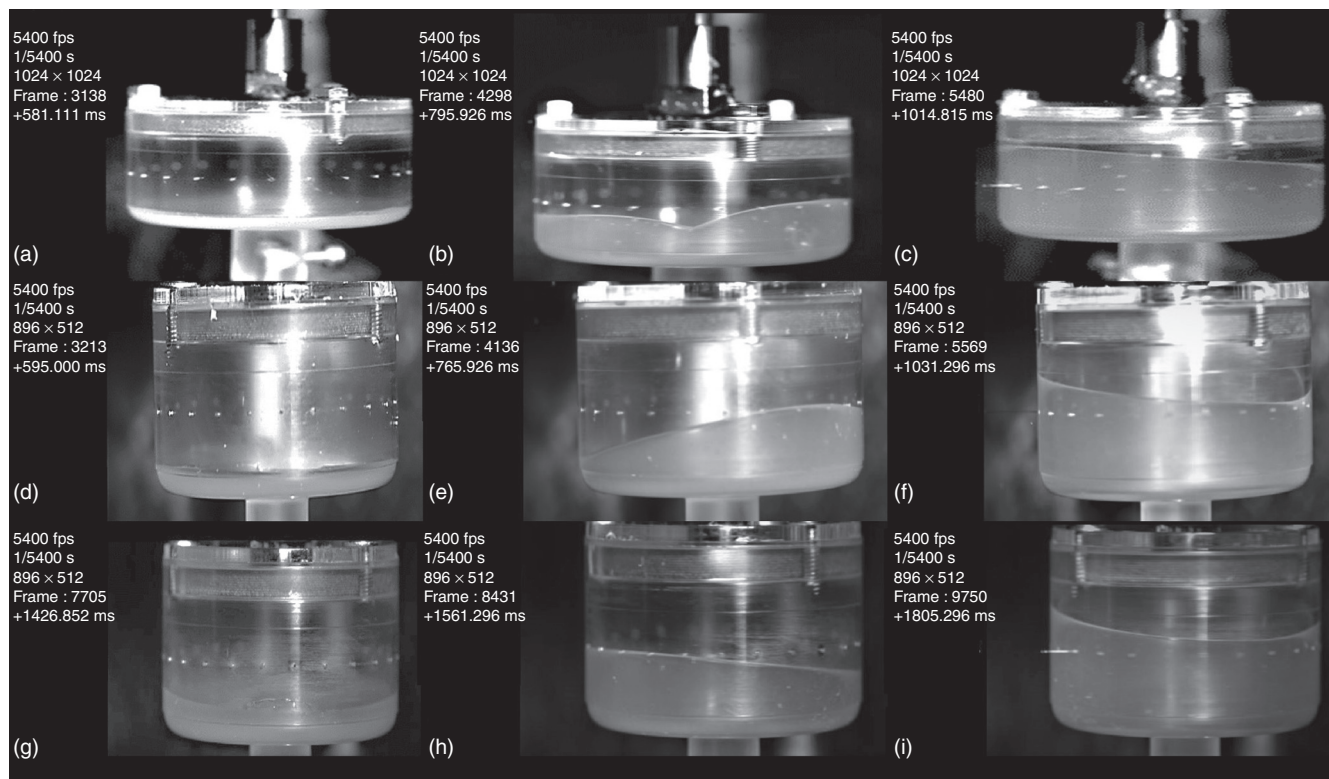


**FIG. 2.** Still pictures obtained from high-speed camera videos: PEO solution at (a)  $\omega = 7000$  rpm at rest, (b)  $t = 215$  ms, (c)  $t = 434$  ms, (d)  $\omega = 8500$  rpm at rest, (e)  $t = 171$  ms, (f)  $t = 436$  ms, (g)  $\omega = 10\,000$  rpm at rest, (h)  $t = 134$  ms, and (i)  $t = 379$  ms.

at a fixed rotating speed. It is clearly shown in Fig. 3(e) that the inlet pressure plays a crucial role in controlling the viscous polymer solution profile, as the fluid arrived at all the orifices at almost the same time and moved upward along the cylinder wall at an equal distance at  $t = 251$  ms. Therefore, in this situation, the jetted solution from the openings had almost equal output speed and altitude. Compared with the previous scenario, the solution jetted out faster by the force of the nitrogen gas escaping from the orifices at high speed, which is described in the numerical results (Sec. III C 4) in more detail. The solution profile was kept controlled at  $t = 349$  ms, as shown in Fig. 3(f) and the polymer solution kept jetting out of the orifices. The fluid did not reach the top surface of the chamber.

*c. PG with 0.3 MPa.* As shown in Figs. 3(g), 3(h), and 3(i), in this case, inlet gas was applied at 0.3 MPa pressure. The time it took the polymer solution to reach the orifices was much shorter at this pressure level compared to the other levels of applied pressure, as shown in Fig. 3(h) ( $t = 205$  ms). Also, the gas pressure forces the liquid to reach the orifices faster than using rotation only. The fluid profile was controlled at the same locations in a parabolic shape, and the solution started jetting from the orifices with the introduction of nitrogen gas, which helped the solution to escape faster. It should be noted here that the high-pressure gas helped the polymer solution to elongate as it exited through the openings, stretching during the separation phase in

particular. Finally, the application of more pressure promoted more control of the polymer solution, which was jetted from all the orifices at the same time in the same amount and at the same speed. As shown in Fig. 3(i), the solution kept the asymmetric shape as it jetted continuously from the chamber, although the polymer solution did not reach the top surface of the cylinder.

## C. Numerical analysis

### 1. Effects of rotational speed at 7000 rpm without gas pressure

Jetting the polymer solution with centrifugal force against the surface tension and gravitational forces led to deformation of the PEO solution at the orifices. In general, a higher spinning speed at a constant pressure leads to higher centrifugal force, which promotes higher solution deformation, as shown in Fig. 4. The viscous PEO solution within the reservoir responds to two forces acting in opposite directions: normal stresses and shear stresses. As a result, the PEO solution elongated with acceleration at the orifices. In the initial condition, the height of the PEO solution was 5 mm, red indicates the PEO solution fraction ( $\phi = 1$ ), and dark blue indicates the air gas fraction ( $\phi = -1$ ) as shown in Fig. 4(a). The shape profile of the surface is not flat, as observed experimentally. Figure 4(b) illustrates the surface profile of the PEO solution inside the chamber at 6 ms and the interface gradients

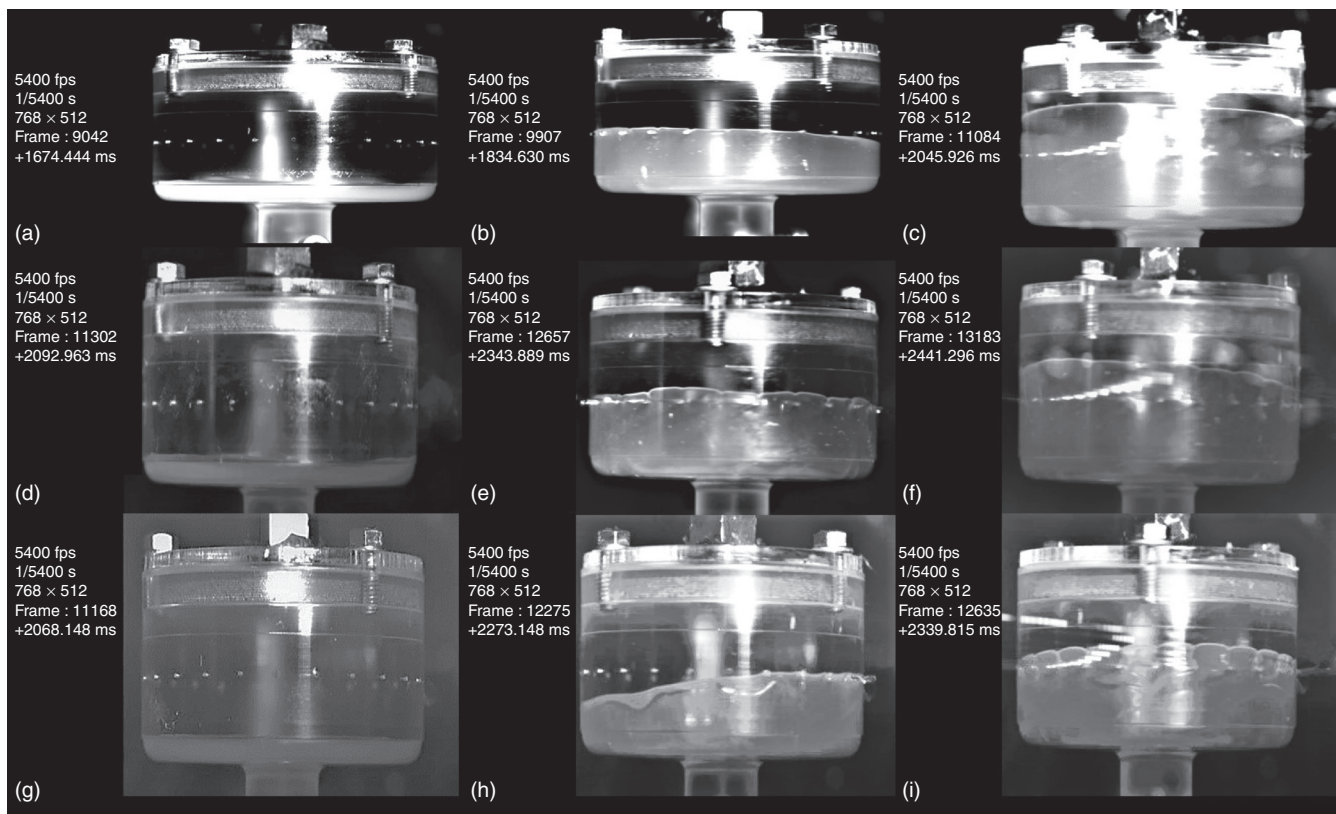


**FIG. 3.** Photograph extracted from high speed camera video recordings: PEO solution at (a)  $\omega = 10\,000$  rpm with 0.1 MPa inlet pressure at rest, (b)  $t = 187$ , (c)  $t = 371$  ms, (d) 10 000 rpm with 0.2 MPa inlet pressure at rest, (e)  $t = 251$  ms, (f)  $t = 349$  ms, (g) 10 000 rpm with 0.3 MPa inlet pressure at rest, (h)  $t = 205$  ms, and (i)  $t = 436$  ms.

of the solution with air within the reservoir. The fluid shifted as expected, and the interface formed a parabolic shape when spun due to centrifugal force; this is theoretically suggested by Eq. (2). It is also clear that the solution reached the orifices when the angular velocity of the cylinder was equal to 7000 rpm. Finally, Fig. 4(c) shows how the PEO solution reached the top surface of the cylinder, and most of the solution was simply jetted out of the vessel at  $t = 20$  ms. The solution profile at this specific time was unsymmetrical near the walls of the reservoir.

## 2. Effects of rotational speed at 8500 rpm without pressure gas

Figure 4(d) shows that the behavior of the polymer solution at a higher speed,  $\omega = 8500$  rpm, at  $t = 6$  ms increased the exit flow from the chamber. It was predicted that in these conditions, the solution at the bottom would move to the sidewalls of the cylinder, compared with the same conditions at  $\omega = 7000$  rpm. An asymmetrical fluid profile was observed for the polymer solution inside the reservoir, which led to fluid escape from some orifices but not others. In Fig. 4(e), it is evident that the polymer solution passed the orifices but did not reach the top surface of the cylinder at  $t = 20$  ms; however, the high volume of the polymer was at the center of the orifices, which led to greater loss of solution that escaped from the openings without fiber formation. As a result, the diameter of the polymer jet was almost the same size and shape as the orifice (0.5 mm); this also affected the produced fibers. At the end of the process, shown in Fig. 4(f), the viscosity of the solution kept the polymer solution above the orifices, which, at that particular time ( $t = 30$  ms), facilitated the high speed of the

air-jetted within the polymer. In turn, this produced a thinner solution that led to a smaller fiber diameter (Sec. III D).

## 3. Effects of rotational speed at 10 000 rpm without gas pressure

At a maximum rotational speed of 10 000 rpm, more fluid withdrawal was observed. In Fig. 4(g) the surface profile and height of the polymer solution at  $t = 6$  ms are illustrated. With high-speed spinning (10 000 rpm), the polymer solution concentrated at the orifices in a shorter time compared to the other speeds tested (i.e.,  $\omega = 7000$  and 8500 rpm), so we can conclude that a higher speed makes the processing time shorter. At  $t = 20$  ms [Fig. 4(h)], unsymmetrical flow distribution was discovered near the cylinder walls, and the volume fraction at the bottom of the chamber was higher than it was at the top and the orifices. However, a low percentage of the polymer solution was located at the top of the reservoir at this speed compared to other speeds at the same time.

The investigation of the polymer solution speed at the orifices showed that this parameter played a vital role in the process. A numerical study of the velocity distribution across the sections inside the cylinder is shown in Figs. 5(a), 5(b), and 5(c) at 7000, 8500, and 10 000 rpm angular velocities, respectively. The spinning speed of the fluid inside the chamber increased gradually from the center to the wall sides, as proven theoretically in Eq. (5). The polymer solution velocity depends on the vessel rotation speed. Therefore, in both cases, the acceleration increased at  $\omega = 8500$  and 10 000 rpm by 22% and 59%, respectively.

The mass flow rate of the PEO solution over time is presented in Fig. 5(d). The maximum values of mass flow rate obtained at

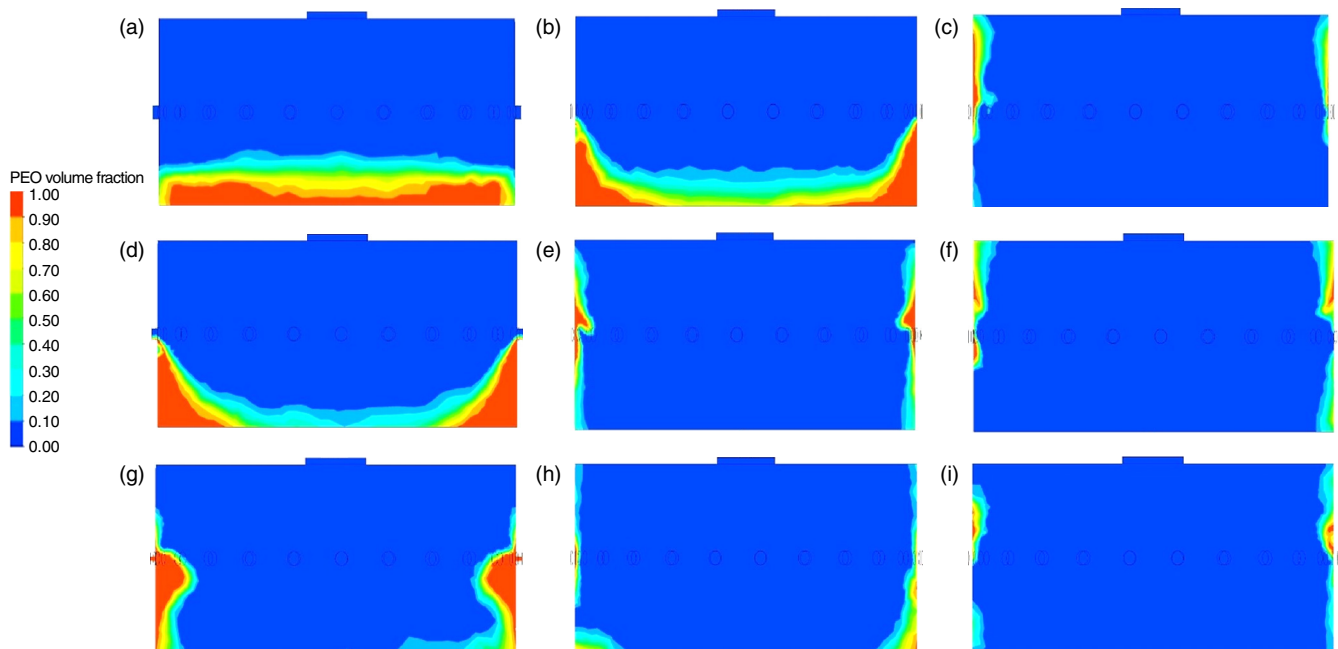


FIG. 4. Photograph extracted from ANSYS-Fluent simulation of PEO solution behavior contours:  $\omega = 7000$  rpm at (a) rest, (b)  $t = 6$  ms, (c)  $t = 20$  ms.  $\omega = 8500$  rpm at (d)  $t = 6$  ms, (e)  $t = 20$  ms, and (f)  $t = 30$  ms.  $\omega = 10\,000$  rpm at (g)  $t = 6$  ms, (h)  $t = 20$  ms, and (i)  $t = 30$  ms.



6(a)–6(c) show the deformation of the PEO solution inside the cylinder under  $P_{\text{inlet}} = 0.1$  MPa at different times (0, 6, and 20 ms). It was observed that the profile of the fluid surface was completely symmetrical under the influence of pressure, and the PEO solution was extracted out from all the orifices; therefore, the produced fibers had the same diameter with acceptable morphology. Figure 6(a) illustrates the fluid surface at the initial condition, where the height of the solution ( $h_{\text{solution}}$ ) was 5 mm. The asymmetric profile of the solution was attained, and the fluid stretched to the orifices after  $t = 6$  ms, as shown in Fig. 6(b). The nitrogen gas forced the polymer solution at the bottom to the interior surfaces side of the orifices, along with the remaining area of the orifices, which affected the speed and flow rate of the polymer solution. This gas also maintained the polymer jet and created a balance between the atmospheric pressure and the nitrogen pressure inside the reservoir, as shown in Fig. 6(c).

In Fig. 6(d), the influence of increased inlet pressure can be seen, as the thickness of the PEO solution at the cylinder walls decreased because of the high inlet gas pressure, which is applied directly downwards at the center of the cylinder. With higher pressure, the fluid reached the orifices after more time had elapsed compared with less pressure because the gas tries to exit from the orifices at the start of the process, as shown in Fig. 6(e). Moreover, the pressure produced by gas distributed the fluid in all points in the center of the orifices with the

same concentration, as shown in Fig. 6(f). As a result, increasing the inlet pressure with nitrogen gas at high speed to assist the fluid jetted into the atmosphere led to a smaller diameter of polymer fiber, which was caused by faster elongation of the jetted solution (Sec. III D).

By increasing the pressure to 0.3 MPa, the PEO solution rapidly moved along the chamber walls at  $t = 6$  ms, as depicted in Fig. 6(g). This strategy also kept the polymer controlled at the center and beneath the orifices, which allowed the solution jetted with nitrogen gas to accelerate the polymer output speed. Figure 6(h) shows the volume of the PEO solution at  $t = 20$  ms, which was concentrated at two locations of the orifice (the top and bottom). Meanwhile, the nitrogen gas in the middle of the orifice expanded the solution, which led to a smaller diameter of solution jetted out from the openings. Figure 6(i) describes the solution behavior at  $t = 30$  ms. The solution was controlled, staying around the orifice, at the bottom of the cylinder, and close to the area above the openings.

Figures 7(a), 7(b), and 7(c) show a numerical study of the velocity distribution inside the chamber at 0.1, 0.2, and 0.3 MPa inlet gas pressure, respectively. The nitrogen gas pressure governed the PEO solution velocity at the inlet of the vessel. Therefore, the velocity rate increased in both cases at 0.2 and 0.3 MPa by 43% and 115%, respectively. The force produced by the nitrogen gas accelerated the solution toward the orifices so that more elongated, thinner fibers were created (Sec. III D).

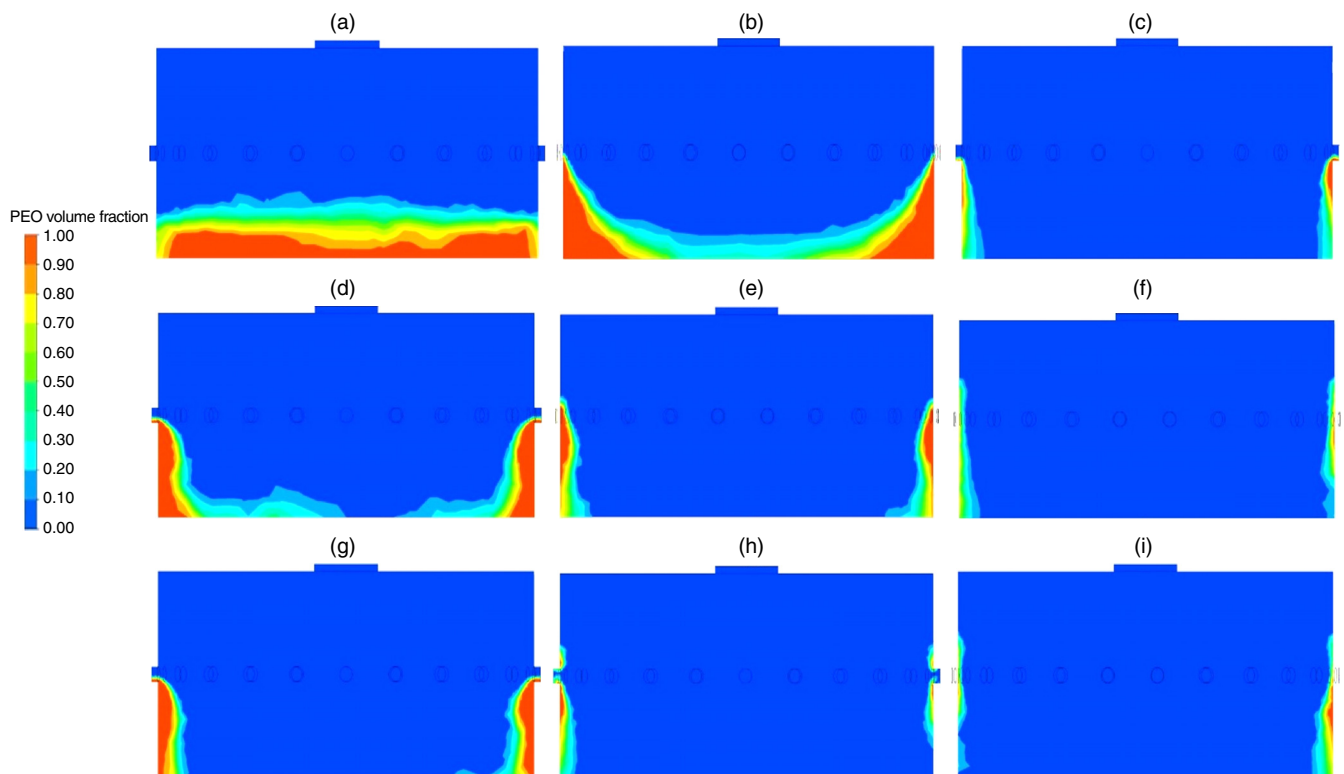


**FIG. 6.** Photographs extracted from ANSYS-Fluent video recording contours of volume fractions of PEO solution at fixed  $\omega = 10\,000$  rpm: at  $P_{\text{inlet}} = 0.1$  MPa at (a) rest, (b)  $t = 6$  ms, and (c)  $t = 20$  ms.  $P_{\text{inlet}} = 0.2$  MPa at (d)  $t = 6$  ms, (e)  $t = 20$  ms, and (f)  $t = 30$  ms. PEO solution volume fraction contour at (g)  $P_{\text{inlet}} = 0.3$  MPa at  $t = 6$  ms, (h)  $t = 20$  ms, and (i)  $t = 30$  ms.

The mass flow rate of the PEO solution is illustrated in Fig. 7(d) at three different pressures: 0.1, 0.2, and 0.3 MPa. The mass flow rate increased excessively with increased inlet pressure; therefore, the inlet gas forced the fluid to exit from the orifices more rapidly and with a greater quantity of PEO solution. The percentages of increase in the mass flow rate compared to inlet pressure at 0.1 MPa were 52% and 29% when 0.3 MPa and 0.2 MPa of gas pressure was applied, respectively. Figure 7(e) illustrates the volume fractions of the PEO solution as a function of time at different pressure levels. The volume fraction decreased with an increase in gas pressure, and the peak of the curve was not clearly observed. The volume fraction of fluid decreased by rates of 25% and 48% for gas pressures of 0.2 and 0.3 MPa, respectively, compared with the volume fraction when the gas pressure was 0.1 MPa. The curve has an obvious parabolic shape, so the numerical results confirm the scenarios elucidated by theoretical Eqs. (1) and (2).

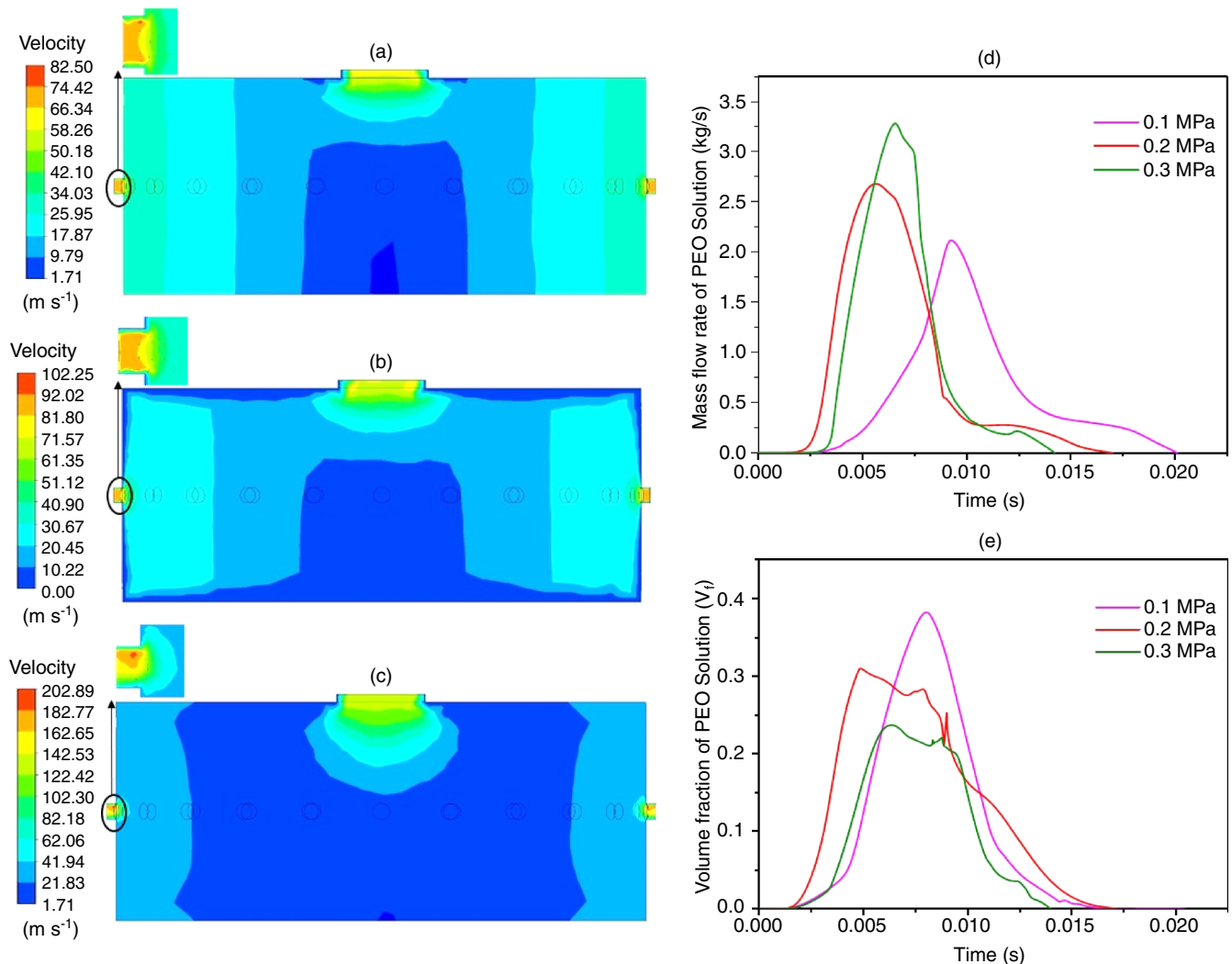


**FIG. 7.** Photograph extracted from ANSYS-Fluent video recording contours of the velocity distribution of PEO solution at fixed  $\omega = 1000$  rpm and (a) at  $P_{inlet} = 0.1$  MPa, (b) at  $P_{inlet} = 0.2$  MPa, and (c) at  $P_{inlet} = 0.3$  MPa. (d) and (e) show mass flow rate and volume fraction, respectively, of PEO solution at  $P_{inlet} = 0.1, 0.2,$  and  $0.3$  MPa vs time.

#### D. Morphology, distribution, and production yield of fibers

Figure 8 shows the characteristics of the fibers formed. The diameter of fibers decreased from  $1625.57 \pm 714.83$  nm to  $1477.06 \pm 368.53$  nm by increasing of speed from 7000 rpm to 10 000 rpm under the same CS conditions. Moreover, the morphology of fibers, homogeneity of fiber distribution, and production yield improved by increasing speed in CS. Bead and droplet defects and nonhomogeneous distribution were observed at 7500 rpm. The morphology of fibers at 10 000 rpm was better than fibers produced at a lower speed, but it was still slightly beaded. The production yield of fibers was 7.9, 8.9, and 11.2 mg per ml solution for 7000, 8500, and 10 000 rpm, respectively.

On the other hand, the fibers produced by PG had a smaller size and better morphology and distribution compared to CS.

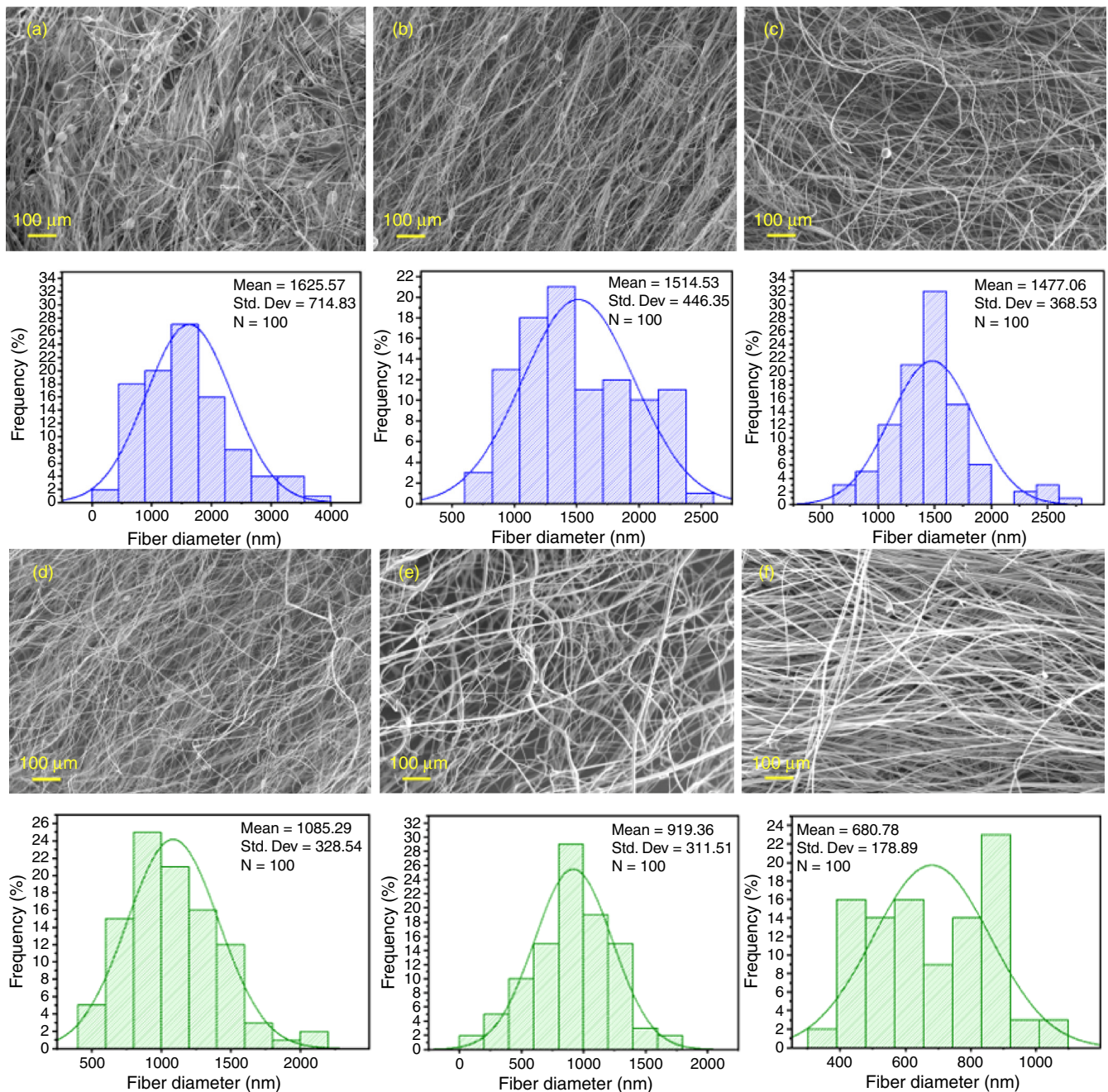


**FIG. 8.** SEM images and fiber diameter distributions of PEO fibers produced by CS at three different speeds: (a) 7000 rpm ( $1625.6 \pm 714.8$  nm), (b) 8500 rpm ( $1514.5 \pm 446.4$  nm), and (c) 10000 rpm ( $1477.1 \pm 368.5$ ); and by PG at three different gas pressures: (d) 0.1 MPa ( $1085.3 \pm 328.5$  nm), (e) 0.2 MPa ( $919.4 \pm 311.5$  nm), and (f) 0.3 MPa ( $680.8 \pm 178.9$  nm).

When we compared PG only, the diameter of fibers decreased from  $1085.29 \pm 328.54$  nm to  $680.78 \pm 178.89$  nm by increasing gas pressure from 0.1 to 0.3 MPa in 10000 rpm under the same PG conditions. The fibers were slightly beaded at 0.1 MPa but the

morphology and homogeneity of fiber distribution improved by increasing the gas pressure to 0.3 MPa. The production yield of fibers was 16.2, 37.7, 54.3 mg per ml solution for 0.1, 0.2, and 0.3 MPa, respectively.

## E. Comparison of experiment and theoretical scenarios

The volume fraction contours in Fig. 4 reveal the behavior of the PEO solution inside the transparent reservoir without any applied pressure (i.e., CS). These contours prove that the polymer solution had a parabolic profile and that it was symmetric at different speeds ( $\omega = 7000, 8500, \text{ and } 10\,000 \text{ rpm}$ ). It was also observed that the polymer solution was jetted from the orifices without fiber formation at a rapid rate, especially at a low rotation speed, as shown in Fig. 4(b), 4(d), and 4(g). However, at  $t = 30 \text{ ms}$ , the solution was jetted with the air outside the chamber and stayed above and below the orifices [Fig. 4(c), 4(f), and 4(i)].

High-speed camera videos were captured in this study to show the same scenario at different times because the numerical study covered a stable, constant speed (i.e., at rest) but not accelerated conditions, which are found in real experiment scenarios. The motor was accelerated to achieve the required speed. This affected not only the time required to reach the orifices but also the symmetry of the fluid profile. The solution escaped from the openings at a lower speed, as shown in Fig. 2, and the fluid was not jetted from the orifices until it reached the top surface. In addition, the mass flow rate, volume fractions, and speed of the polymer solution as it exited from the orifices increased with an increased spinning speed, as shown in Fig. 5.

In the PG process, pressure played a crucial role by controlling the polymer solution within the cylinder; this was proven experimentally and numerically. As Fig. 3 shows, at different speeds, the inlet pressure controlled the solution within the reservoir and jetted the polymer fluid with high-speed gas, which increased the speed of the fluid and elongated the polymer at the exit of the orifices. Furthermore, Fig. 6 shows how the fluid profile was controlled inside the cylinder, staying around the orifices when jetted with nitrogen gas at all times.

The main purpose of this work was to elucidate how the polymeric fluid behaves during pressurized gyration and pressureless centrifugal spinning, comparing the scenarios. Overall, higher spinning speed and pressure will help decrease fiber diameter. However, automated control of the speed, pressure, and flow of polymer solution is needed to achieve fine fibers with a monomodal diameter distribution, and to further decrease the fiber diameter higher values of pressure and speed need to be tested. We are currently designing and testing a novel vessel-device, which can be computer-controlled with respect to automation and will also tolerate higher pressure and speed.

## IV. CONCLUSIONS

An experimental investigation was conducted with high-speed camera imaging, in combination with a numerical analysis (CFD), to examine the fluid behavior in two systems: PG and CS for forming polymeric fine fibers. 21 wt. % PEO dissolved in distilled water as a viscous solution was used in two scenarios. The first scenario used CS at three speeds without any applied pressure, and it was concluded that increasing the spinning speed allowed the polymer solution to jet out of the orifices faster. With a higher speed, the fluid rapidly formed into a parabolic shape and moved to the reservoir walls; it then continued to move upward to the top surface of the cylinder and, as a result, fluid started to jet out of the cylinder. Numerically, the ratio of the speed at which the solution escaped at 8500 and 10 000 rpm compared to 7000 rpm equaled 22% and 59%, respectively. The greatest quantity of

polymer was formed at the beginning of the process from 0.002 to 0.05 s. The percentages of the total process time at 8500 and 10 000 rpm were 56% and 39% less than the time consumed at 7000 rpm, respectively.

In the PG scenario, three levels of inlet pressure were applied (0.1, 0.2, and 0.3 MPa) at a fixed spinning speed of 10 000 rpm. The inlet pressure played a vital role at all spinning speeds and was crucial for effectively controlling the fluid profile within the reservoir. At the same time, the inlet gas helped the polymer solution reach the orifices in a short time (less than 1 s) and kept the fluid at the same location within the cylinder, which allowed the fluid to jet at the same time from all the orifices. Also, nitrogen gas was jetted with the solution out of the orifices at high speed to allow the polymer to stretch and evaporate the water.

There was a strong relationship between the magnitude of pressure applied and the speed at which the solution escaped from the orifices, which led to improved fiber morphology. The morphology of fibers, homogeneity of fiber distribution, and production yield improved by increasing the spinning speed in CS but was further enhanced by increasing the gas pressure. The best results were obtained at 0.3 MPa in PG. Finally, the total process time was less than 1 s in both the experimental and numerical studies. In future work, the process will be controlled by an automated system that allows the polymer solution to infuse into the chamber at a suitable spinning speed to reduce the amount of solution waste and to ensure an accurate volume flow rate for both the polymer solution and the inlet gas, which play a vital role in forming fine polymer fibers.

## SUPPLEMENTARY MATERIAL

See the [supplementary material](#) for further details about videos extracted from high-speed camera recording of PEO solution behavior using the centrifugal spinning (CS) technique at 7000 rpm (Supplementary Video 1), 8500 rpm (Supplementary Video 2), and 10 000 rpm (Supplementary Video 3). The videos extracted from a high-speed camera during the use of the pressurized gyration technique (PG) at 0.1 MPa (Supplementary Video 4), 0.2 MPa (Supplementary Video 5), and 0.3 MPa (Supplementary Video 6) are provided. Additionally, videos obtained from ANSYS-Fluent recording of PEO solution behavior in CS at 7000 rpm (Supplementary Video 7), 8500 rpm (Supplementary Video 8), and 10 000 rpm (Supplementary Video 9), as well as in PG at 0.1 MPa (Supplementary Video 10), 0.2 MPa (Supplementary Video 11), and 0.3 MPa (Supplementary Video 12) are included.

## ACKNOWLEDGMENTS

The authors are grateful to the U.K. Engineering & Physical Sciences Research Council (EPSRC) for funding pressurized gyration forming research at University College London (Grant Nos. EP/S016872/1, EP/N034228/1, and EP/S016872/1). Hussain Alenezi wishes to thank PAAET-Kuwait for sponsoring his Ph.D. research (Grant No. 278010301647). Dr. Muhammet E. Cam was supported by a TUBITAK 2219 Research Program Grant (Scientific and Technological Research Council of Turkey-TUBITAK) and thanks UCL Mechanical Engineering, for hosting his post-doctoral research in the U.K. We also thank Peter Kelly, Phil Jeavons of the UCL Mechanical Engineering Workshop for their suggestions and help in pressurized gyraxion vessel design and making.

## REFERENCES

- <sup>1</sup>Kenry and C. T. Lim, *Prog. Polym. Sci.* **70**, 1 (2017); A. Shapira, N. Noor, M. Asulin, and T. Dvir, *Appl. Phys. Rev.* **5**(4), 041112 (2018).
- <sup>2</sup>H. Cho, S.-Y. Min, and T.-W. Lee, *Macromol. Mater. Eng.* **298**(5), 475 (2013); K. P. De Jong and J. W. Geus, *Catal. Rev.* **42**(4), 481 (2000); C.-M. Hsu and S. Shivkumar, *Macromol. Mater. Eng.* **289**(4), 334 (2004); N. Bhardwaj and S. C. Kundu, *Biotechnol. Adv.* **28**(3), 325 (2010); S. Ramakrishna, K. Fujihara, W.-E. Teo, T. Yong, Z. Ma, and R. Ramaseshan, *Mater. Today* **9**(3), 40 (2006); G. L. Bezemer, J. H. Bitter, H. P. C. E. Kuipers, H. Oosterbeek, J. E. Holewijn, X. Xu, F. Kapteijn, A. J. van Dillen, and K. P. de Jong, *J. Am. Chem. Soc.* **128**(12), 3956 (2006); M. Zhu, J. Han, F. Wang, W. Shao, R. Xiong, Q. Zhang, H. Pan, Y. Yang, S. K. Samal, F. Zhang, and C. Huang, *Macromol. Mater. Eng.* **302**(1), 1600353 (2017); B. Yoon and S. Lee, *Fiber Polym.* **12**(1), 57 (2011); M. W. Lee, S. An, C. Lee, M. Liou, A. L. Yarin, and S. S. Yoon, *J. Mater. Chem. A* **2**(19), 7045 (2014); J. Xie, M. R. MacEwan, W. Liu, N. Jesuraj, X. Li, D. Hunter, and Y. Xia, *ACS Appl. Mater. Interfaces* **6**(12), 9472 (2014).
- <sup>3</sup>X. Hong, S. Mahalingam, and M. Edirisinghe, *Macromol. Mater. Eng.* **302**(6), 1600564 (2017).
- <sup>4</sup>C. J. Luo, S. D. Stoyanov, E. Stride, E. Pelan, and M. Edirisinghe, *Chem. Soc. Rev.* **41**(13), 4708 (2012).
- <sup>5</sup>A. Wilson, BCC Research (2018).
- <sup>6</sup>M. Gagliardi, BCC Research (2019).
- <sup>7</sup>P. L. Heseltine, J. Ahmed, and M. Edirisinghe, *Macromol. Mater. Eng.* **303**(9), 1800218 (2018).
- <sup>8</sup>M. Wehmann and W. J. G. McCulloch, in *Polypropylene: An A-Z Reference*, edited by J. Karger-Kocsis (Springer, Dordrecht, Netherlands, 1999), pp. 415.
- <sup>9</sup>P. X. Ma and R. Zhang, *J. Biomed. Mater. Res.* **46**(1), 60 (1999).
- <sup>10</sup>M. He, J. Xue, H. Geng, H. Gu, D. Chen, R. Shi, and L. Zhang, *Appl. Surf. Sci.* **335**, 121 (2015); J. Malberg, T. Wiegand, H. Eckert, M. Bodensteiner, and R. Wolf, *Chem Eur. J.* **19**(7), 2356 (2013); P. Soldate and J. Fan, *J. Appl. Phys.* **125**(5), 054901 (2019).
- <sup>11</sup>P. B. McDaniel, J. M. Deitzel, and J. W. Gillespie, *Polymer* **69**, 148 (2015); T. Nguyen Dang, I. Richard, E. Goy, F. Sordo, and F. Sorin, *J. Appl. Phys.* **125**(17), 175301 (2019).
- <sup>12</sup>J. Wang and D. Zhang, *Adv. Polym. Technol.* **32**(S1), E323 (2013).
- <sup>13</sup>N. Anantharamaiah, P. D. Svetlana Verenich, and B. Pourdeyhimi, *J. Eng. Fibers Fabr.* **3**(3), 1 (2008).
- <sup>14</sup>R. P. R. Nayak, I. L. Kyratzis, Y. B. Truong, and L. Arnold, *Text. Res. J.* **82**(2), 129 (2011).
- <sup>15</sup>K. Sarkar, C. Gomez, S. Zambrano, M. Ramirez, E. de Hoyos, H. Vasquez, and K. Lozano, *Mater. Today* **13**(11), 12 (2010).
- <sup>16</sup>P. Mellado, H. A. McIlwee, M. R. Badrossamay, J. A. Goss, L. Mahadevan, and K. K. Parker, *Appl. Phys. Lett.* **99**(20), 203107 (2011).
- <sup>17</sup>S. Mahalingam and M. Edirisinghe, *Macromol. Rapid Commun.* **34**(14), 1134 (2013).
- <sup>18</sup>M. R. Badrossamay, H. A. McIlwee, J. A. Goss, and K. K. Parker, *Nano Lett.* **10**(6), 2257 (2010).
- <sup>19</sup>S. Mahalingam, B. T. Raimi-Abraham, D. Q. M. Craig, and M. Edirisinghe, *Langmuir* **31**(2), 659 (2015); R. T. Weitz, L. Harnau, S. Rauschenbach, M. Burghard, and K. Kern, *Nano Lett.* **8**(4), 1187 (2008).
- <sup>20</sup>X. Xu and J. Luo, *Appl. Phys. Lett.* **91**(12), 124102 (2007).
- <sup>21</sup>B. T. Raimi-Abraham, S. Mahalingam, M. Edirisinghe, and D. Q. Craig, *Mater. Sci. Eng. C* **39**, 168 (2014).
- <sup>22</sup>F. M. Chen and X. Liu, *Prog. Polym. Sci.* **53**, 86 (2016).
- <sup>23</sup>K. Devanand and J. C. Selser, *Nature* **343**(6260), 739 (1990).
- <sup>24</sup>S. Padron, A. Fuentes, D. Caruntu, and K. Lozano, *J. Appl. Phys.* **113**(2), 024318 (2013); A. Valipouri, S. A. H. Ravandi, A. Pishevar, and E. I. Părău, *Int. J. Multiphase Flow* **69**, 93 (2015).
- <sup>25</sup>X. Hong, A. Harker, and M. Edirisinghe, *ACS Omega* **3**, 5470 (2018).